

Provided for non-commercial research and educational use only.
Not for reproduction or distribution or commercial use.



This article was originally published in a journal published by Elsevier, and the attached copy is provided by Elsevier for the author's benefit and for the benefit of the author's institution, for non-commercial research and educational use including without limitation use in instruction at your institution, sending it to specific colleagues that you know, and providing a copy to your institution's administrator.

All other uses, reproduction and distribution, including without limitation commercial reprints, selling or licensing copies or access, or posting on open internet sites, your personal or institution's website or repository, are prohibited. For exceptions, permission may be sought for such use through Elsevier's permissions site at:

<http://www.elsevier.com/locate/permissionusematerial>

Discrete and continuum modelling of excavator bucket filling

C.J. Coetzee^{a,*}, A.H. Basson^a, P.A. Vermeer^b

^a *Department of Mechanical Engineering, University of Stellenbosch, Private Bag X1, 7602 Matieland, South Africa*

^b *Institut für Geotechnik, Universität Stuttgart, Pfaffenwaldring 35, D-70569 Stuttgart, Germany*

Received 15 March 2006; received in revised form 18 July 2006; accepted 25 July 2006

Available online 4 October 2006

Abstract

Two-dimensional discrete and continuum modelling of excavator bucket filling is presented. The discrete element method (DEM) is used for the discrete modelling and the material-point method (MPM) for continuum modelling. MPM is a so-called particle method or meshless finite element method. Standard finite element methods have difficulty in modelling the entire bucket filling process due to large displacements and distortions of the mesh. The use of a meshless method overcomes this problem. DEM and MPM simulations (plane strain) of bucket filling are compared to two-dimensional experimental results. Cohesionless corn grains were used as material and the simulated force acting on the bucket and flow patterns were compared with experimental results. The corn macro (continuum) and micro (DEM) properties were obtained from shear and oedometer tests. As part of the MPM simulations, both the classic (nonpolar) and the Cosserat (polar) continua were used. Results show that the nonpolar continuum is the most accurate in predicting the bucket force while the polar and DEM methods predict lower forces. The DEM model does not accurately predict the material flow during filling, while the polar and nonpolar methods are more accurate. Different flow zones develop during filling and it is shown that DEM, the polar and the nonpolar methods can accurately predict the position and orientation of these different flow zones.

© 2006 ISTVS. Published by Elsevier Ltd. All rights reserved.

Keywords: Discrete element method; Material-point method; Cosserat continuum; Bucket filling; Digging process; Excavation

1. Introduction

Earthmoving equipment is not only used for mining, it also plays an important role in the agricultural and earthmoving industries. The equipment is highly diverse in shape and function, but most of the soil cutting machines can be categorised into one of three principal classes: blades, rippers and buckets or shovels. The basic shape of earthmoving tools has not changed a great deal since antiquity, although most are operated today by mechanical power sources and their construction benefits from modern metallurgical engineering.

A dragline excavator is a crane-like structure with a huge bucket of up to 100 m³ in volume. These machines are used to remove blasted overburden from open cast mines to expose the coal deposits beneath for mining. Draglines are an expensive and essential part of mine operations. In the South African coal mining industry it is generally accepted that a 1% improvement in the efficiency of a dragline will result in an R 1 million increase in annual production per dragline [1].

The problem of soil–tool interaction has been solved using limit analysis by a number of researchers (e.g. [2–4]). A number of boundary value problems have been solved using these methods, but they are limited to infinitesimal motion of the tool and given geometry of the problem [5]. These methods were not expected to be valid for the analysis of the subsequent stages of advanced earth digging problems.

* Corresponding author. Tel.: +27 21 808 4239.

E-mail address: ccoetzee@sun.ac.za (C.J. Coetzee).

The process of excavator bucket filling was investigated experimentally by the group of Maciejewski [5,6]. The aim of their research is optimisation of the digging process and investigating the effect of the number and position of teeth on bucket performance.

No publication on the modelling of bucket filling using a continuum method, such as the finite element method (FEM), could be found. Bucket filling involves large displacements and deformations which are difficult to model with classic finite element methods due to the distortion of the mesh. For this research, bucket filling is modelled using the so-called meshless finite element method (material-point method, MPM) which overcomes the problem of mesh distortions. FEM also has difficulty in detecting and resolving contact between deformable bodies. Special contact elements and algorithms are needed. A special MPM contact algorithm makes the modelling of Coulomb friction contact between deformable bodies possible at low computational cost.

A totally different approach, the discrete element method (DEM), is also used to model bucket filling. The forces acting on the bucket and the material flow patterns, as predicted by these two methods, are compared to experimental results and observations.

1.1. Discrete modelling

The discrete element methods are based on the simulation of the motion of granular material as separate particles. DEM was first applied to soils by Cundall and Strack [7]. Calculations performed during a DEM simulation alternate between the application of Newton's second law to the particles and a force-displacement law at the contacts. DEM has the advantage that it can easily be used for the simulation of granular flow subjected to large deformations and free boundaries. The main problem with DEM is how to specify the micro-properties (particle contact properties) so that the flow on macro-level of thousands of particles behaves in the same way as real granular flow. Laboratory experiments (e.g. shear tests, biaxial tests and oedometer tests) are necessary to determine these properties before any useful modelling and predictions can be made. Cleary [8] modelled dragline bucket filling using DEM. Trends were shown and qualitative comparisons made, but no experimental results were presented.

1.2. Continuum modelling

Although meshless methods originated about twenty years ago, little research effort has been devoted to them until recently. Particle methods can be characterised as methods where the solution variables are attributed to Lagrangian point masses (particles) instead of computational cells [9].

Sulsky et al. [10] developed a particle method (called the material-point-method) applicable to solid mechanics that

can be used to model impact, penetration and large deformations. MPM uses two discretisations of the material, one based on a computational mesh and the other based on a collection of material points or 'particles'. This approach combines the advantages of Eulerian and Lagrangian descriptions of the material while avoiding the shortcomings of each. The equations of motion are solved in a Lagrangian frame on a computational grid, using standard finite element methods. Convection is modelled by moving the material points in the computed velocity field. Each material point carries its material properties without error while it is moved. Since all the state variables are assigned to the numerical material points, the information carried by these points is enough to characterise the flow and the grid carries no permanent information. Thus, the grid can be discarded and reconstructed for computational convenience each time step. See Appendix A for details.

In granular materials the discreteness of the system is often important and rotational degrees of freedom are active, which might require enhanced theoretical approaches like polar continua [11]. The concept of polar continua naturally brings a length scale into the continuum theory.

In polar continuum theories, the material points are considered to possess orientations. A material point has three degrees-of-freedom for rigid rotations, in addition to the three classic translational degrees-of-freedom. Eringen [12] describes polar continua in detail. The Cosserat continuum is the most transparent and straightforward extension of classic or nonpolar continuum models and was proposed by E. and F. Cosserat in 1909 [13]. The non-polar constitutive laws must be adapted to include the rotational degrees-of-freedom which leads to new laws such as polar elasticity and polar plasticity. The rotations are induced by couple stresses within the continuum. The presence of couple stresses results in a stress tensor which is no longer symmetric as in the case of a nonpolar continuum.

In this paper, the results from MPM simulations are compared to the DEM and experimental results. The MPM method used, is based on both the classic continuum and the Cosserat continuum formulations.

2. Experimental and numerical setup

Two-dimensional experiments were performed by moving a bucket profile between two glass panels 200 mm apart. The forces acting on the bucket were measured and the flow patterns could be observed. The bucket used in the experiments was a dragline type of bucket. The bucket was given a constant drag velocity (horizontal) of 10 mm/s. The effective weight of the bucket could be adjusted through a system of linkages and a counterweight. The bucket was free to move in the vertical direction. The effective bucket weight and the flow of material into the bucket caused the bucket to dig into the material. The path of motion was recorded and used as input for the DEM and MPM models. The bucket had a total length of

approximately 350 mm. For a detailed description of the experimental setup and data acquisition see Coetzee [14,15].

Rowlands [16] observed that seed grains are suitable for experimental testing and closely resemble natural granular flow into dragline buckets. The grains have a relatively low friction coefficient with glass, which makes it a good material for experiments. The seed grains were also found suitable for DEM simulations because the stiffness of the grains is less than the stiffness of, say, gravel. The smaller stiffness results in a larger time step and decreases the total computing time [14]. For a close-packed assembly, the stable time step is roughly inversely proportional to the particle stiffness [17]. Coetzee [14] used direct shear and oedometer tests to determine the corn properties to be used for the DEM and MPM simulations.

A Drucker–Prager constitutive model [18] was used for nonpolar modelling and a polar Drucker–Prager model [19] for polar modelling. The corn grains had an average size of more or less 10 mm. The characteristic length used in the polar continuum, assumed this value [19]. The moment of inertia was calculated by assuming a cylinder with a diameter equal to the characteristic length. Plane strain conditions were assumed. Maciejewski [6] investigated the flow behaviour in a test bench similar to the one used for this research, and concludes that the assumption of plane strain conditions is valid. The other material properties are summarised in Table 1. The bucket was modelled as a rigid body.

In the DEM model, initial conditions were generated by allowing material to fall from a fixed height along the total length of the test rig [14]. In the MPM model, the 2.0×0.7 m domain was divided into 200×100 rectangular elements, each of size 10×7 mm. The bottom boundary was fixed in the horizontal, vertical and rotational (polar only) directions and the two side boundaries in the horizontal and rotational (polar only) directions. The boundaries were far away from the bucket and had no significant effect on the results. Polar rotation was not

allowed at the bucket–material interface [19]. The material stresses were initialised using a coefficient of earth pressure $K_0 = 1 - \sin \phi$ [20]. The bucket was placed on top of the material with the tooth engaged.

3. Results

Fig. 1 shows the measured, nonpolar MPM, polar MPM and DEM draft force acting on the bucket. The nonpolar MPM draft force corresponds well to the measured force up to a displacement of 600 mm, but thereafter it underpredicts the force and at 800 mm the error is 12%. The DEM predicted force is 20 N lower than the measured force up to a displacement of 600 mm. Polar MPM predicts a draft force which is lower than both the measured force and the nonpolar predicted force.

Figs. 2 and 3 show the experimental, DEM, nonpolar MPM and polar MPM filling process at increments of 200 mm in bucket displacement. From these pictures it is difficult to compare the flow. These pictures were digitised and the shape of the free surface, as predicted by the different methods, plotted on the same figure (Fig. 4).

During the initial stages of filling, there is an upheave of material right above the tooth. Up to a displacement of 200 mm the nonpolar continuum predicts the free surface and the upheave the most accurately while the polar continuum predicts less upheave of material during these initial stages of filling. Between the displacements of 400 mm and 600 mm, the polar continuum predicts the free surface more accurately than the nonpolar continuum. Compared to the experimental free surface, the DEM model predicts less upheave of material during the entire filling process.

Rowlands [16] made use of mixtures of millet, peas and corn in his test rig which is similar to the one used here. The observation of the filling behaviour led to the development of a theory that describes the flow characteristics and

Table 1
Material properties

	Symbol	Corn
<i>Continuum macro properties</i>		
Young's modulus	E	2.76 MPa
Poisson's ratio	ν	0.2
Density	ρ	778 kg m^{-3}
Friction angle	ϕ	26°
Dilatancy angle	ψ	2°
Cohesion	c	0 Pa
Cosserat shear modulus	$G^c = 2G$	2.3 MPa
Characteristic length	l	10 mm
Particle moment of inertia	$J_{33} = 0.5(0.5l)^2$	$12.5 \times 10^{-6} \text{ m}^2$
Friction with steel	ϕ_s	14°
<i>DEM micro properties</i>		
Particle stiffness	$k_n = k_s$	420 kN m^{-1}
Particle density	ρ_p	855 kg m^{-3}
Particle friction	μ	0.1

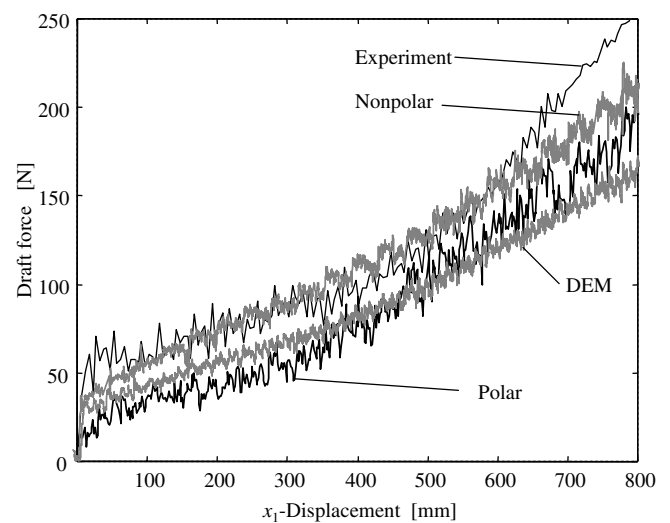


Fig. 1. Bucket draft force as measured and predicted by nonpolar mpm, polar MPM and DEM.

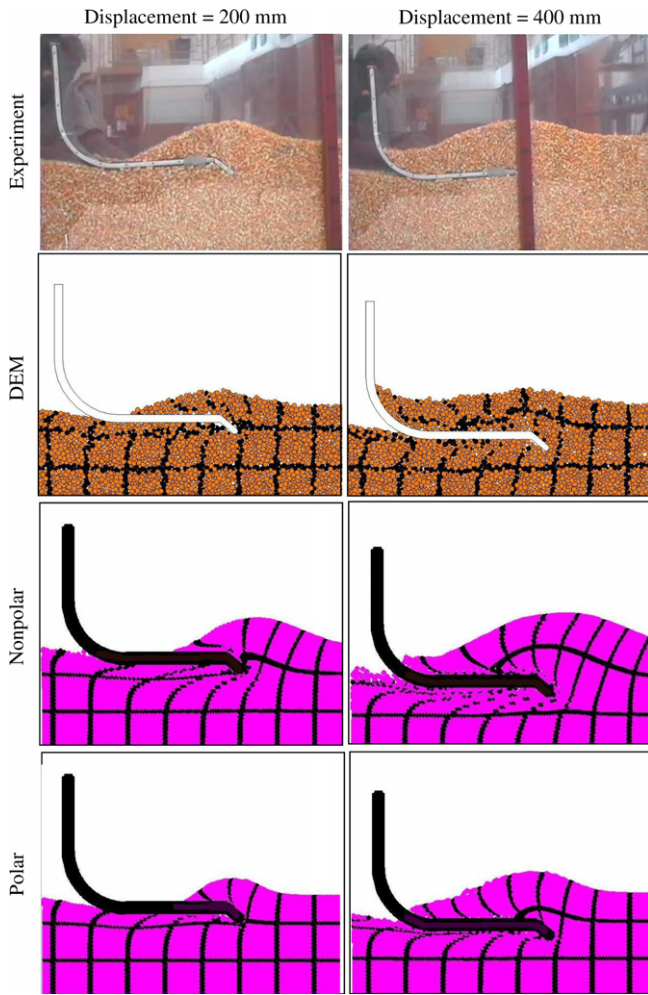


Fig. 2. The flow of corn into the bucket: displacement 200 mm and 400 mm.

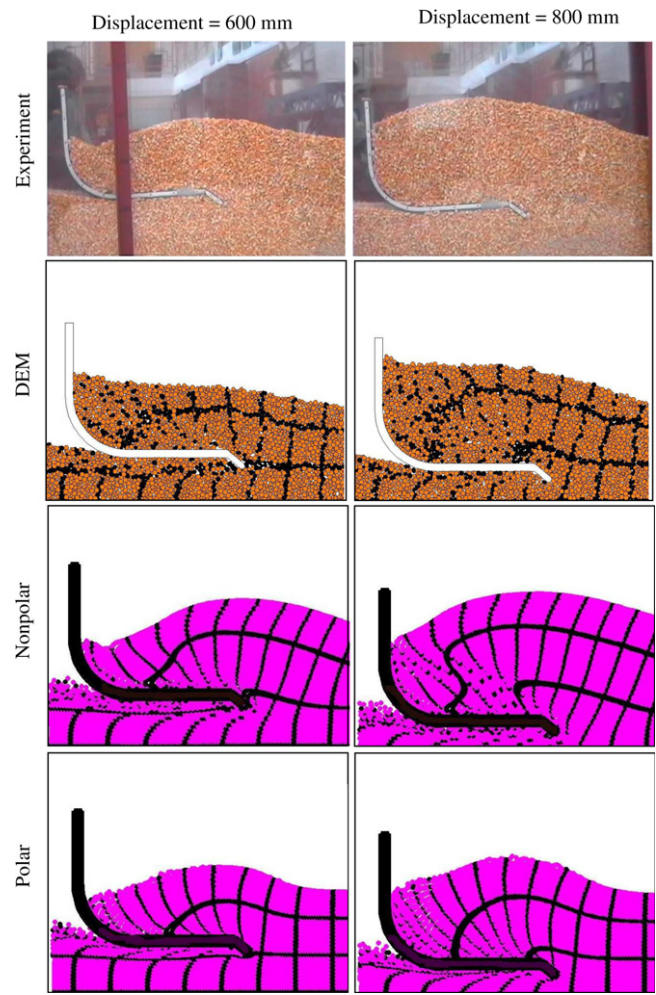


Fig. 3. The flow of corn into the bucket: displacement 600 mm and 800 mm.

patterns of material entering the bucket. Rowlands [16] named this concept the shear zone theory. Maciejewski [6] used material with cohesion and could also identify specific flow regions. Rowlands observed that definite planes of shear formed between distinct moving material regimes. These shear planes changed orientation and location depending on initial setup and during the filling process itself.

The generalised theory is illustrated in Fig. 5. The movements of the material relative to the bucket are indicated by the arrows. The virgin material remains largely undisturbed until the final third of the drag during which “bulldozing” occurs. The initial laminar layer flows into the bucket during the first third of the drag. After entering to a certain distance, this layer fails at the bucket lip and subsequently becomes stationary with respect to the bucket for the remainder of the drag. With the laminar layer becoming stationary, a new zone, the active flow zone, develops. In this zone, the material displacement is predominantly in the vertical direction. The active dig zone is located above the teeth and bucket lip. This area develops as material starts to enter the bucket and increases in size after failure

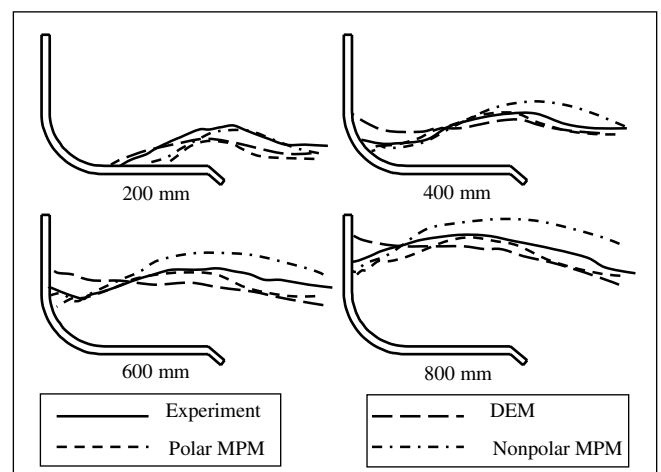


Fig. 4. Comparison of the free surface of the material flowing into the bucket.

of the initial laminar layer. In this zone, the virgin material fails and either flows into the bucket as part of the laminar layer during the first part of filling or moves into the active

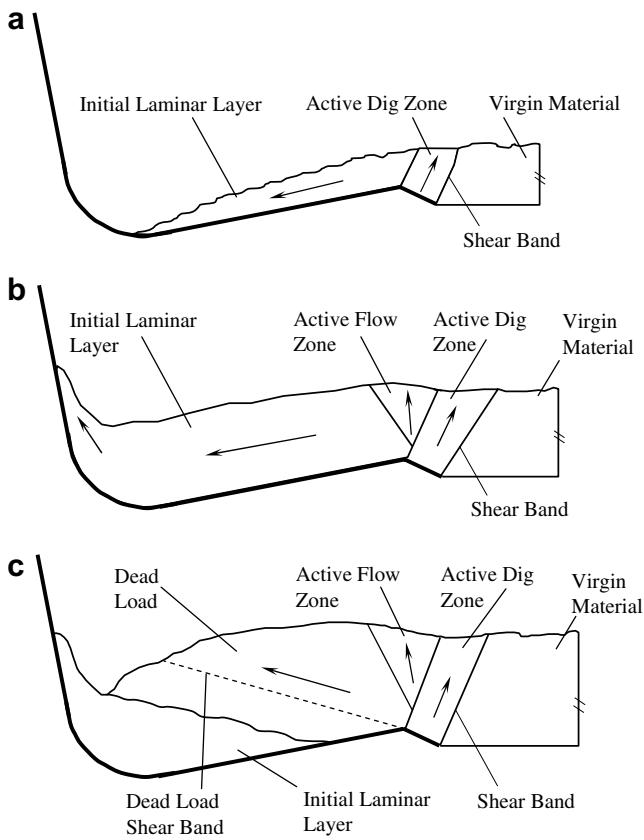


Fig. 5. The Shear zone theory [16].

flow zone during the latter part of filling. The dead load that has resulted from “live” material in the active flow zone ramps up and over the initial laminar layer. Some of the material in the initial laminar layer fails and starts to form part of the dead load.

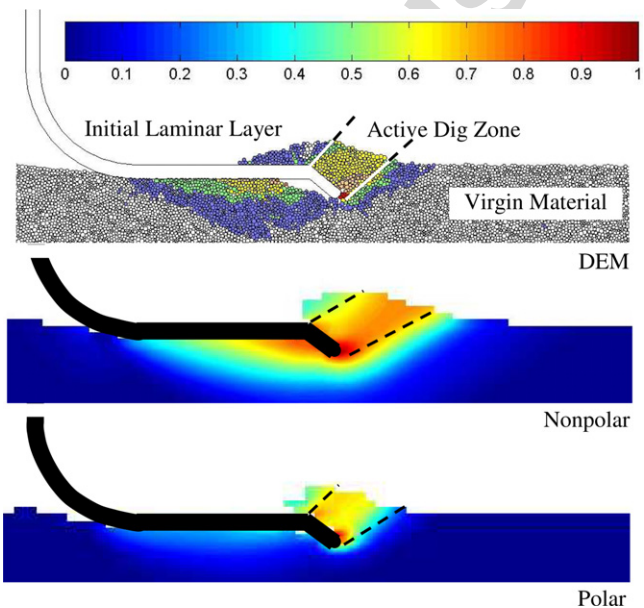


Fig. 6. The Shear zone theory at a displacement of 100 mm.

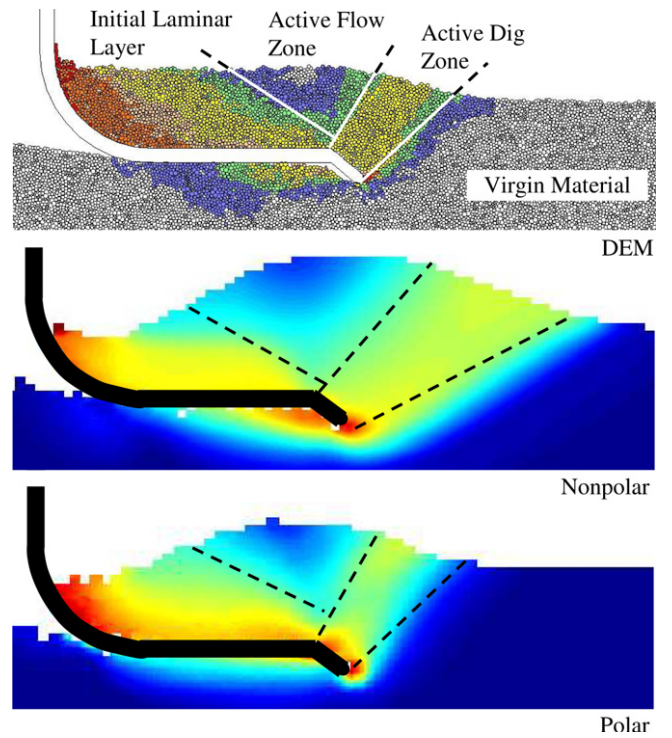


Fig. 7. The Shear zone theory at a displacement of 500 mm.

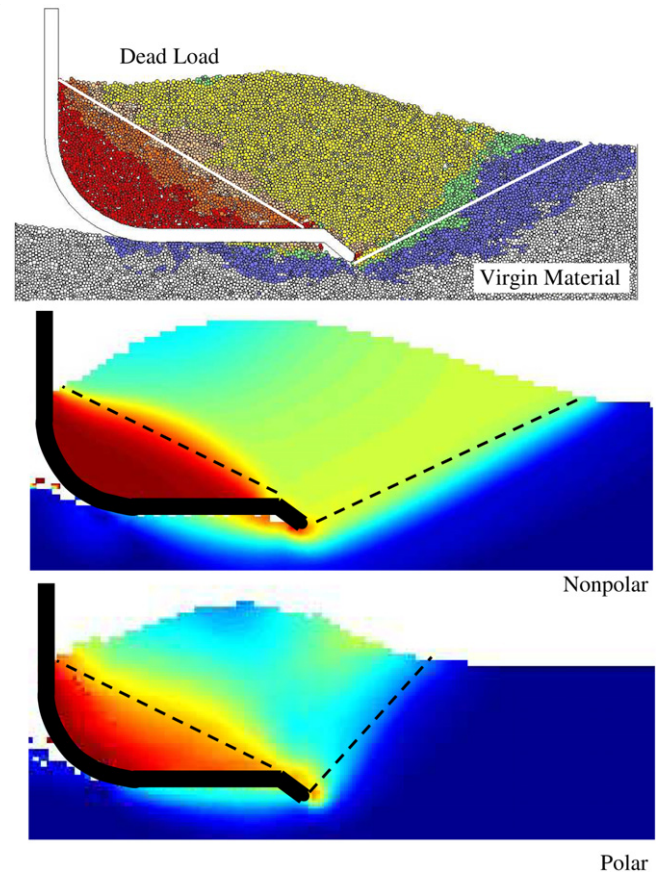


Fig. 8. The Shear zone theory at a displacement of 800 mm.

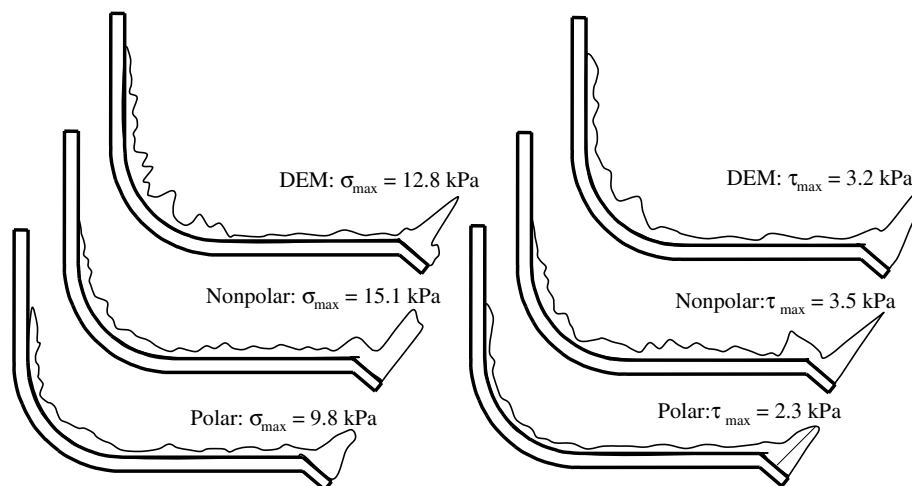


Fig. 9. The normal and shear stress on the inside of the bucket at a displacement of 800 mm.

During the experiments two shear bands could be observed. The one extended from the tip of the tooth up to the free surface. This is known as the cutting shear band. The second line is the one between the initial laminar layer and the dead load, called the dead load shear band. The dead load shear band stretches from the tooth up to the free surface with an angle close to the material internal friction angle. This is indicated by the dotted line in Fig. 5.

To investigate the ability of DEM to predict the shear zone theory, the particle displacement ratio, PDR, is defined. The bucket was moved through the material and “paused” after each 100 mm. The displacement vector of each particle (DEM) or material point (MPM) was then set to be zero after which the bucket was given a further displacement of 10–15 mm. The particles/material points were then coloured according to their PDR values which is defined as the ratio of the magnitude of the particle displacement vector to the bucket displacement vector. A PDR of unity means that the particle moves with the bucket, and a PDR of zero means that the particle has not moved. The results are shown in Figs. 6–8 for displacements of 100 mm, 500 mm and 800 mm. All three methods (DEM, polar and nonpolar MPM) are capable of predicting the different flow zones, although the orientation of the shear bands between the zones differ slightly. The characteristic V-shape of the active flow zone is predicted by all three methods.

The prevention of excessive wear on buckets plays a very important role in bucket design. Special replaceable wear packages are designed and added to buckets which increases the bucket weight. In order to minimise and predict bucket wear, the contact forces or pressures at the bucket-material interface should be known. From a DEM model all the particle-bucket contacts are known. The contact position, normal and tangential forces and the particle velocity are available at each contact and can be used to predict bucket wear. Thirty to forty years ago Finnie [21,22] developed a simple model for predicting

wear. The model essentially uses the kinetic energy of the incoming particle and knowledge about the impact angle to predict wear rates. Cleary [8] modelled bucket filling with DEM and made use of the Finnie model to predict the wear. Realistic wear patterns were obtained, but no experimental data was available for comparisons of the flow patterns, drag forces, wear patterns and wear rates.

Fig. 9 shows the normal (σ) and shear (τ) stresses on the inside of the bucket. For the DEM models the contact normal and shear forces were used to calculate the stress, while for the MPM models the nodal forces were used. The maximum stresses occur on the tooth as expected. The DEM predicted stresses are in general lower than the nonpolar predicted stress and the polar predicted stress lower than both the nonpolar and DEM predicted stress. It is difficult to verify these values experimentally, and further work is needed to find a correlation between wear rates and contact pressures.

4. Conclusion

DEM and MPM simulations were compared to experiments of bucket filling using cohesionless corn grains. The MPM models made use of polar and nonpolar Drucker–Prager constitutive models. All three methods predicted the trend in drag force during filling accurately. Quantitatively, nonpolar MPM is the most accurate while the polar MPM and DEM models predict drag forces lower than the measured.

The DEM model did not accurately predict the material flow during filling. It fails to model the upheave of material directly above the tooth. The polar and nonpolar MPM methods predict the free surface more accurately than DEM. The DEM model depends on the parameters used and more accurate parameter values might result in the DEM model being more accurate in predicting the material flow. The DEM package used does not include rolling resistance. Several authors [23] have shown that rolling resistance can have a significant effect on the

modelled behaviour of granular materials. Direct shear tests showed that the DEM material has an internal friction angle within $\pm 1^\circ$ of the measured and the inclusion of rolling resistance would result in higher frictional strength. How much rolling resistance would influence the modelling of bucket filling is a topic that needs further research.

All three methods accurately predicted the different flow regions that develop as material enters the bucket. The characteristic V-shape of the active flow zone was predicted by all the methods, although the orientation and positions of the different zones differed slightly.

It is shown that the normal and shear stresses on the bucket surface can be determined. This was, however not compared to measurements. During further work, the contact stresses could be used to predict wear rates and wear patterns.

Finally it is concluded that DEM and MPM can successfully model excavator bucket filling. This process is difficult to model with conventional FEM due to large displacements and severe distortion of the mesh. When a relatively small number of particles is used in a DEM simulation, computing times are comparable to that of MPM. However, when the number of particles used are relatively high (100,000+), the time to complete a DEM simulation would increase. In this case, it would be advantageous to use MPM. In this paper, a cohesionless material is used. When cohesion is added, it becomes more difficult to determine the DEM particle properties. Cohesion can, however, easily be added to the MPM models as this is already included in the constitutive models used, but set to zero in the cases analysed here.

Appendix A. The material-point method

In the first part of this section, index notation is used to denote vectors and matrices. The subscripts i, j and k are used, assuming values of 1, 2 and 3, unless stated otherwise. In the latter part of the appendix, Hassenpflug [24] notation is used. A column vector is indicated by a overbar, \bar{x} , a row vector by a underbar, \underline{x} and a matrix by both, $\underline{\underline{x}}$. Plane strain conditions are assumed.

A.1. Space discretisation

First, the initial configuration of the body is divided into a number of subregions. This is done as depicted in Fig. A1. In the centre of each subregion a material point or particle is placed. This material point represents the subspace, and is given a mass m_p . The mass is calculated by assuming that the whole mass of the subregion is concentrated at the material point. The mass of a material point is constant and does not change with time or position. The density $\rho(x_i)$ represented by this collection of discrete mass points is approximated using the Dirac delta function

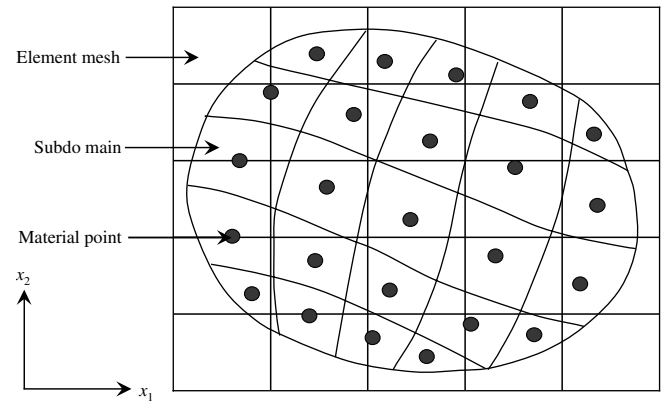


Fig. A1. The element mesh and material points (particles) within the subdomains.

$$\rho(x_i) = \sum_{p=1}^{N_p} m_p \delta(x_i - x_i^p) \quad (\text{A.1})$$

where x_i is an arbitrary position vector, x_i^p is the position vector at material point p , N_p is the total number of material points and the Dirac delta function is defined as follows:

$$\delta(x - a) = \begin{cases} 0 & x \neq a \\ \infty & x = a \end{cases} \quad \text{and} \quad \int_{-\infty}^{+\infty} \delta(x - a) dx = 1 \quad (\text{A.2})$$

For clarity, the equations of motion are derived for a single element only. The whole system would be analysed by assembling the matrices and vectors as in standard FEM routines. The mass of each material point is fixed which ensures mass conservation.

The weak form of the linear momentum equation is given by

$$\int_V \rho \frac{dv_i}{dt} w_i dV = \int_V \rho f_i w_i dV - \int_V \rho \sigma_{ij}^s w_{i,j} dV + \int_S \tau_i w_i dS \quad (\text{A.3})$$

where v_i is the velocity vector, f_i the body forces and τ_i the surface traction acting on surface S and w_i is test function. σ_{ij}^s is the specific stress tensor defined as the Cauchy stress tensor divided by the material density. Substitution of the discrete density representation, Eq. (A.1), into Eq. (A.3) and making use of the definition of the Dirac delta function yields an discrete expression where the integration is performed as a sum of material point properties.

$$\sum_{p=1}^{N_p} m_p \frac{dv_i^p}{dt} w_i^p = \sum_{p=1}^{N_p} m_p f_i^p w_i^p - \sum_{p=1}^{N_p} m_p \sigma_{ij}^{sp} w_{i,j}^p + \int_S \tau_i w_i dS \quad (\text{A.4})$$

The superscript p indicates a variable evaluated at the material point. For example, the specific stress $\sigma_{ij}^{sp} \equiv \sigma_{ij}^{sp}(x_i^p)$.

A.2. Element formulation

The element mesh used is similar to that of FEM. Four noded quadrilateral elements are used. Under the assumption of two-dimensional conditions, the acceleration field $\dot{v}_i \equiv \frac{dv_i}{dt}$, for example, can be written in terms of nodal- and shape function-values

$$\dot{\mathbf{v}}(\bar{\mathbf{x}}, t) \equiv [\dot{v}_1 \dot{v}_2]^T = \bar{\mathbf{N}} \dot{\mathbf{v}}^n \quad (\text{A.5})$$

where $\bar{\mathbf{N}}$ is a matrix containing the shape functions. The element nodal acceleration vector, $\dot{\mathbf{v}}^n$, contains the nodal values of the acceleration field. The same can be applied to the vector field w_i to obtain a vector $\bar{\mathbf{w}}$. Define the following vectors under plane strain conditions,

$$\bar{\boldsymbol{\sigma}}^s \equiv \begin{bmatrix} \sigma_{11}^s \\ \sigma_{22}^s \\ \sigma_{12}^s \end{bmatrix}, \quad \bar{\mathbf{f}} \equiv \begin{bmatrix} f_1 \\ f_2 \end{bmatrix}, \quad \bar{\boldsymbol{\tau}} \equiv \begin{bmatrix} \tau_1 \\ \tau_2 \end{bmatrix} \quad (\text{A.6})$$

with $\sigma_{12}^s = \sigma_{21}^s$. Note that under the assumption of plane strain, the third normal stress component σ_{33}^s is not included in the definition above. This component is, however, calculated at each material point and used in the constitutive model. Using these definitions, Eq. (A.4) can be written as follows:

$$\begin{aligned} \bar{\mathbf{w}}^T \sum_{p=1}^{N_p} m_p (\bar{\mathbf{N}}^p)^T \bar{\mathbf{N}}^p \dot{\mathbf{v}}^n &= \bar{\mathbf{w}}^T \sum_{p=1}^{N_p} m_p (\bar{\mathbf{N}}^p)^T \bar{\mathbf{F}}^p - \bar{\mathbf{w}}^T \\ &\times \sum_{p=1}^{N_p} m_p (\bar{\mathbf{B}}^p)^T \bar{\boldsymbol{\sigma}}^{sp} + \bar{\mathbf{w}}^T \\ &\times \int_S (\bar{\mathbf{N}}^p)^T \bar{\boldsymbol{\tau}} dS \end{aligned} \quad (\text{A.7})$$

where the superscript p indicates values to be evaluated at the material points, e.g. $\bar{\mathbf{N}}^p \equiv \bar{\mathbf{N}}(\bar{\mathbf{x}}^p)$. The arbitrary test vector $\bar{\mathbf{w}}$ appears in all the above terms and can thus be dropped. The final discretised system of equations follows as

$$\bar{\mathbf{M}} \dot{\mathbf{v}}^n = \bar{\mathbf{F}}^{\text{int}} + \bar{\mathbf{F}}^{\text{ext}} \quad (\text{A.8})$$

where the mass matrix $\bar{\mathbf{M}}$ is given by

$$M_{ij} \equiv \bar{\mathbf{M}} = \sum_{p=1}^{N_p} m_p (\bar{\mathbf{N}}^p)^T \bar{\mathbf{N}}^p \quad (\text{A.9})$$

the internal force vector is given by

$$F_i^{\text{int}} \equiv \bar{\mathbf{F}}^{\text{int}} = - \sum_{p=1}^{N_p} m_p (\bar{\mathbf{B}}^p)^T \bar{\boldsymbol{\sigma}}^{sp} \quad (\text{A.10})$$

and the external force vector is given by

$$F_i^{\text{ext}} \equiv \bar{\mathbf{F}}^{\text{ext}} = \int_S (\bar{\mathbf{N}}^p)^T \bar{\boldsymbol{\tau}} dS \quad (\text{A.11})$$

The matrix $\bar{\mathbf{B}}^p$ contains shape function gradients. In practice, to simplify computations, a lumped mass matrix may be used instead of the consistent mass matrix given

by Eq. (A.9). The lumped mass matrix is a diagonal matrix with each entry being the corresponding row sum of the consistent mass matrix. Matrix inversions become trivial if a lumped matrix is used, at the cost of introducing a small amount of numerical dissipation [25,26]. The consistent mass matrix can also be singular for certain arrangements of the particles. There appears to be only a few arrangements of particles that yield a singular consistent mass matrix, but nearby arrangements might result in an ill-conditioned matrix. On the other hand, the lumped matrix is diagonal and well conditioned.

A.3. Time integration

Let the time step size be Δt . The solution to the system of Eq. (A.8) is found at discrete instants in time $t, t+1, \dots, t+n$. The calculation during each time increment consists of three phases; a initialisation phase, a Lagrangian phase and a convective phase [27].

A.3.1. Initialisation phase

Assume that the position and velocity vector, stress tensor, strain tensor and history dependent variables of each material point are known at time t . With the position of each particle known, its shape function values can be computed and hence the mass matrix, $\bar{\mathbf{M}}^t$, given by Eq. (A.9). Mapping of the particle velocities to the nodes, provides the initial data for the solution to Eq. (A.8). The following equation is solved to obtain the nodal velocity $\bar{\mathbf{v}}^{n,t}$ at time t .

$$\bar{\mathbf{M}}^t \bar{\mathbf{v}}^{n,t} = \sum_{p=1}^{N_p} m_p (\bar{\mathbf{N}}^p)^T \begin{bmatrix} v_1^{p,t} \\ v_2^{p,t} \end{bmatrix} \quad (\text{A.12})$$

where $[v_1^{p,t} \ v_2^{p,t}]^T$ is the material point velocity vector at time t , containing the velocity components in the x_1 - and x_2 -directions, respectively. This equation expresses equivalence of momentum calculated for the material points and for the nodes [28].

A.3.2. Lagrangian phase

With the shape functions of each particle known, the internal- and external-force vectors can be calculated using Eqs. (A.10) and (A.11), respectively. With these two vectors and the mass matrix known, Eq. (A.8) is solved for the nodal acceleration at time t .

$$\dot{\mathbf{v}}^{n,t} = (\bar{\mathbf{M}}^t)^{-1} (\bar{\mathbf{F}}^{\text{int},t} + \bar{\mathbf{F}}^{\text{ext},t}) \quad (\text{A.13})$$

The “new” nodal velocity, $\bar{\mathbf{v}}^{n,t+1}$, at time $t+1$ is obtained by using an explicit time integrator

$$\bar{\mathbf{v}}^{n,t+1} = \bar{\mathbf{v}}^{n,t} + \Delta t \dot{\mathbf{v}}^{n,t} \quad (\text{A.14})$$

which obviously requires very small time steps to ensure accuracy. Using the new nodal velocity, the increment in strains can be calculated at the particles. Define the vector of strain increment as follows:

$$\Delta \bar{\boldsymbol{\epsilon}}^p \equiv [\epsilon_{11}^p \ \epsilon_{22}^p \ \epsilon_{12}^p]^T \quad (\text{A.15})$$

This vector can be calculated using matrix $\bar{\mathbf{B}}^{p,t}$

$$\Delta \bar{\boldsymbol{\varepsilon}}^{p,t+1} = \Delta t \bar{\mathbf{B}}^{p,t} \bar{\mathbf{v}}^{n,t+1} \quad (\text{A.16})$$

With the increment in strain known, the new stress state $\bar{\boldsymbol{\sigma}}^{p,t+1}$ at each material point can be calculated based on the chosen constitutive model. One way of doing this, would be to calculate the stress increment, using the tangent modulus $\bar{\mathbf{M}}^{p,t}$

$$\Delta \bar{\boldsymbol{\sigma}}^{p,t+1} = \bar{\mathbf{M}}^{p,t} \Delta \bar{\boldsymbol{\varepsilon}}^{p,t+1} \quad (\text{A.17})$$

The use of the tangent modulus in a numerical algorithm, however, results in a tendency for the stress to drift from the yield surface [10]. In practice a incremental iterative scheme is rather used. With the given increment in strain, the material is assumed to be elastic, and a trial stress state is computed. The yield function f is evaluated using the trial state, and if $f \leq 0$ the material point is still in the elastic region and no further calculations are needed. However, if $f > 0$, return algorithms, based on the flow potential g , are needed to force f back to zero. In the case of a Mohr–Coulomb or Drucker–Prager model, a simple one-step return to the yield surface is possible [18]. For other models like Lade, a iterative procedure is needed.

History dependent variables such as strain-hardening parameters may also be updated at this stage. During the Lagrangian phase the nodes are assumed to move at the computed nodal velocity $\bar{\mathbf{v}}^{n,t+1}$. Thus, points in the interior of the element move in proportion to the motion of the nodes, as given by the representation using the nodal shape functions. Since shape functions are used to map the nodal velocity continuously to the interior of the element, the positions of the material points are updated by moving them in a single-valued, continuous velocity field. Similarly, the velocity of a material point is updated by mapping the nodal accelerations to the material point position. The updated position vector and velocity vector follow as

$$\bar{\mathbf{x}}^{p,t+1} = \bar{\mathbf{x}}^{p,t} + \Delta t \bar{\mathbf{N}}^{p,t} \bar{\mathbf{v}}^{n,t+1}; \quad \bar{\mathbf{v}}^{p,t+1} = \bar{\mathbf{v}}^{p,t} + \Delta t \bar{\mathbf{N}}^{p,t} \dot{\bar{\mathbf{v}}}^{n,t} \quad (\text{A.18})$$

Because the velocity field is single-valued, interpenetration of material is precluded. This feature of the algorithm allows simulations of impact and penetration without the need for a special contact algorithm.

A.3.3. Convective phase

At this point in the computational cycle, the material points are completely updated and carry the complete solution, i.e., all the state variables needed to start a new calculation step are carried by the material points. During the convective phase, the material points are held fixed and the element mesh can be redefined. The mesh can be chosen in any convenient manner, for example adaptive meshes can be used to resolve sharp gradients and interfaces. The simplest and most convenient choice is, however, to keep the existing mesh. Any motion of the mesh relative to the material points model convection. Since the material points do not move during the convective phase, material point

properties have the same value at the end of the convective phase as they had at the end of the Lagrangian phase. This completes the computational cycle. A new cycle is begun using the information carried by the material points to initialise nodal values on the element mesh.

A.4. Stability

In the previous sections, a simple explicit time integrator is used of which the time step should satisfy the stability condition, i.e. the critical time step should be the smallest ratio of the element size to the wave speed through the material. For small displacements, the spatial discretisation in MPM is equivalent to that of FEM using Gauss points at the same locations as those of the material points in each element. Therefore, the convergence behaviour of the integrator used is similar to that employed to integrate the corresponding equations in FEM. However, according to Chen et al. [29], no consistent theoretical results have been obtained for the convergence behaviour of time integrators when larger deformations occur and a reasonable time step is usually found through numerical experiments.

A.5. Contact model

The MPM formulation presented here automatically enforces no-slip contact between two different bodies. The reason for this is that a single-valued velocity field is used for updating the particle positions. Bardenhagen et al. [30], however, developed an algorithm which relaxes the no-slip condition and allows Coulomb friction and slip at contacting boundary nodes. This contact algorithm was implemented to model the bucket-soil interface. The friction angle between the corn and the steel bucket is given in Table 1.

The bucket was modelled as a continuum following a rigid body material model. The material points defining the bucket geometry were given a constant velocity and allowed to move through the mesh like all other material points. Using the contact algorithm by Bardenhagen et al., coulomb friction was allowed at nodes common to the bucket and the granular material. The theory behind the contact model is not presented here and the reader is referred to Bardenhagen et al. [30].

References

- [1] Esterhuysen SWP. The influence of geometry on dragline bucket filling performance. MSc thesis, Mechanical Engineering, University of Stellenbosch, Stellenbosch, South Africa; 1997.
- [2] Dechao Z, Yusuf Y. A dynamic model for soil cutting by blade and tine. *J Terr* 1992;29(3):317–27.
- [3] Osman MS. The mechanics of soil cutting blades. *J Agric Eng Res* 1964;9(4):313–28.
- [4] Swick WC, Perumpral JV. A model for predicting soil–tool interaction. *J Terr* 1988;25(1):43–56.
- [5] Maciejewski J, Jarzebowski A. Laboratory optimization of the soil digging process. *J Terr* 2002;39:161–79.

- [6] Maciejewski J, Jarzebowski A, Trampczynski W. Study on the efficiency of the digging process using the model of excavator bucket. *J Terr* 2004;40:221–33.
- [7] Cundall PA, Strack ODL. A discrete numerical method for granular assemblies. *Geotechnique* 1979;29:47–65.
- [8] Cleary PW. The filling of dragline buckets. *Math Eng Ind* 1998;7(1):1–24.
- [9] Benson DJ. Computational methods in Lagrangian and Eulerian hydrocodes. *Comput Method Appl M* 1992;99:235–394.
- [10] Sulsky D, Zhou S-J, Schreyer HL. Application of a particle-in-cell method to solid mechanics. *Comput Phys Commun* 1995;87:236–52.
- [11] Herrmann H. Institute for computer applications: Physics on supercomputers, University of Stuttgart, ICA1 Annual Report, 1999.
- [12] Eringen CA. *Microcontinuum field theories, I: Foundations and solids*. New York: Springer; 1999.
- [13] de Borst R. Simulation of strain localization: a reappraisal of the Cosserat continuum. *Eng Comput* 1991;8:317–32.
- [14] Coetzee CJ. *Forced granular flow*. MSc thesis, Mechanical Engineering, University of Stellenbosch, Stellenbosch, South Africa; 2000.
- [15] Coetzee CJ. *The modelling of granular flow using the particle-in-cell method*. PhD thesis, Mechanical Engineering, University of Stellenbosch, Stellenbosch, South Africa; 2004.
- [16] Rowlands JC. *Dragline bucket filling*. PhD thesis, University of Queensland, Queensland, Australia; 1991.
- [17] Itasca. *PFC2D: User manual: Theory and background, Version 2.0; 1998*. Available from: www.itascacg.com.
- [18] *FLAC, fast Lagrangian analysis of continua: theory and background; 1998*. Available from: www.itascacg.com.
- [19] Teichman J. *Modelling of shear localisation and autogeneous dynamic effects in granular bodies*, des Institutes fur Bodenmechanik und Felsmechanik der Universitat Fridericiana in Karlsruhe; 1997.
- [20] Jaky J. The coefficient of earth pressure at rest. *J Soc Hungarian Arch Eng* 1944(October):355–8.
- [21] Finnie I. Erosion of surfaces by solid particles. *Wear* 1960;3:87–103.
- [22] Finnie I. Some observations on the erosion of ductile metals. *Wear* 1972;19:81–90.
- [23] Iwashita K, Oda M. Rolling resistance at contacts in simulation of shear band development by DEM. *J Eng Mech* 1998;124(3):285–92.
- [24] Hassenpflug WC. Matrix tensor notation part I: rectilinear orthogonal coordinates. *Comput Math Appl* 1993;26(3):55–93.
- [25] Burgess D, Sulsky D, Brackbill JU. Mass matrix formulation of the FLIP particle-in-cell method. *J Comput Phys* 1992;103:1–15.
- [26] Brackbill JU, Kothe DB, Ruppel HM. A low dissipation particle-in-cell method for fluid flow. *Comput Phys Commun* 1988;48:25–38.
- [27] Sulsky D, Chen Z, Schreyer H. A particle method for history-dependent materials. *Comput Methods Appl Mech Eng* 1994;118:179–96.
- [28] Wieckowski Z. Analysis of granular flow by the material point method. In *European conference on computational mechanics June 26–29, Cracow, Poland; 2001*.
- [29] Chen Z, Hu W, Shen L, Xin X, Brannon R. An evaluation of the MPM for simulating dynamic failure with damage diffusion. *Eng Fract Mech* 2002;69:1873–90.
- [30] Bardenhagen SG, Brackbill JU, Sulsky DL. The material-point method for granular materials. *Comput Methods Appl Mech Eng* 2000;187:529–41.